

Single-Nanoparticle Resolved Biomimetic Long-Range Electron Transfer and Electrocatalysis of Mixed-Valence Nanoparticles

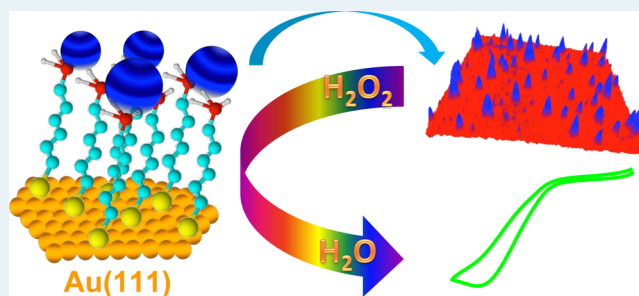
Nan Zhu, Xian Hao, Jens Ulstrup, and Qijin Chi*

Department of Chemistry, Technical University of Denmark, Kemitorvet Building 207, DK-2800 Kongens Lyngby, Denmark

S Supporting Information

ABSTRACT: Long-range electron transfer (LRET) is a core elementary step in a wealth of processes central to chemistry and biology, including photosynthesis, respiration, and catalysis. In nature, biological catalysis is performed by enzymes. However, enzymes are structurally fragile and have limited stability *in vitro*. Development of robust biomimetic nanostructures is therefore highly desirable. Here, with Prussian blue nanoparticles (PBNPs) as an example we have demonstrated the preparation of highly stable and water-soluble mixed-valence nanoparticles under mild conditions. We have mapped their enzyme-mimicking catalytic properties and controlled LRET to single-nanoparticle resolution. PBNPs show high substrate binding affinity and tunable electrocatalytic efficiency toward hydrogen peroxide reduction, resembling the patterns for similar size redox metalloenzymes. We have further disclosed a correlation between electrocatalytic efficiency and distance-dependent interfacial ET kinetics. Given their high stability and low cost, such enzyme-mimicking nanoparticles could offer new perspectives in the fields of catalysis, sensors, and electrochemical energy conversion.

KEYWORDS: biomimetic nanoparticles, redox-active nanoparticles, enzyme-mimicking electrocatalysis, Prussian blue, distance controlled electron transfer, two-dimensional surface self-assembly



1. INTRODUCTION

Nanoparticles (NPs) dominate a wide range of nanostructures with different chemical compositions, sizes, and morphologies. New types of NPs have been created over the past two decades, with particular efforts toward controlling their size, shape, crystal structure, and functionality. A recent review highlights the current status and future perspectives of NP-based nanoscience and nanotechnology.¹ High priority is given to develop further NP-based biotechnology and nanomedicine. In this context, novel design and synthesis as well as an understanding of the fundamental behavior of biomimetic NPs are of particular interest.

Biomimetic NPs with physicochemical properties that resemble those of natural macromolecules (e.g., proteins and enzymes), have become attractive to both scientific communities and industry, because of their low cost and high stability in comparison to natural biological macromolecules.^{1,2} These biomimetic NPs can be designed as “smart” components and assembled into versatile nanomaterials with desirable functionalities.^{3,4} One of the most intriguing examples is enzyme-mimicking structures.² Enzyme-like inorganic metallic or metal oxide NPs are expected to display efficient biocatalysis and, at the same time, high stability and low cost toward industrial production. Such NPs can be used for a range of purposes: for example, as catalysts in biosensing and energy conversion.^{5,6}

Electrocatalysis is an essential process in a wealth of chemical and biological systems. Electrocatalytic processes have been

widely explored for their applications in organic synthesis,^{7,8} fuel cells,^{9,10} and biosensors.^{11,12} In particular, the electrocatalytic reduction of dioxygen, hydrogen peroxide (H_2O_2), and carbon dioxide is of current crucial importance in biosensing technology, energy conversion, and environmental engineering. The development of electrocatalysts is, however, currently approached at the nanoscale. Understanding electrocatalysis with the resolution of the single NPs is thus becoming a critical focus for matching a variety of challenges in the rational design of high-performance electrocatalysts.^{13–15} In many applications, NPs need to be immobilized on a specific support material, where their performance strongly depends on the surface properties of both the electrocatalysts and support materials. The support materials mostly used are electrochemical electrodes of metals, metal oxides, and various carbon materials. Among a large family of mixed-valence transition-metal complex materials, Prussian blue (PB) is regarded as the first coordination chemical compound, known for over three centuries. PB materials have continued to pose new challenges regarding their structural, electronic, and electrochemical properties as well as new biocatalytic perspectives. As an electroactive material, PB has proven to be of broad interest for electrochemical sensors and biosensors by acting as an ET

Received: February 9, 2016

Revised: March 14, 2016

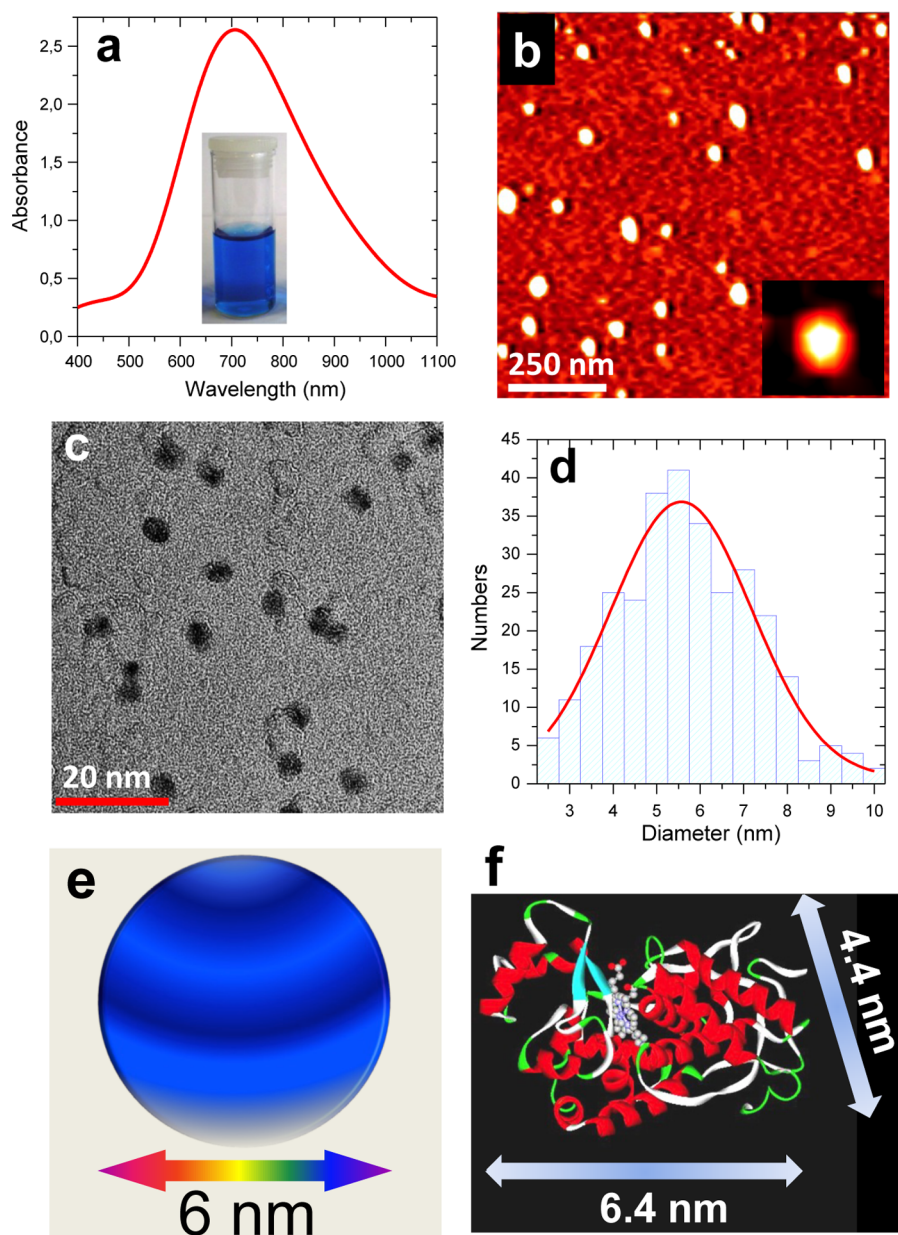


Figure 1. Synthesis and characterization of 5–6 nm Prussian blue nanoparticles: (a) UV–vis spectrum of a PBNP dispersed solution with a photograph of the solution in the inset; (b) AFM image of PBNPs deposited physically on mica surfaces recorded in air; (c, d) TEM image and the PBNP size distribution; (e) schematic illustration of a single PBNP with the size emphasized; (f) three-dimensional structural representation of horseradish peroxidase as a size comparison with PBNP.

mediator.^{16–22} While electrodeposited PB polycrystalline thin films have been intensely investigated,^{16–22} much fewer reports have focused on nanometer-size PBNPs^{23–25} that can offer unique physical and chemical properties in comparison with their bulk counterparts. Achieving a controlled ET process and studying electrocatalytic efficiency at the single-NP level has remained elusive but could be feasible by the use of pure PBNPs and interdisciplinary instrumental methods.

We have proven the feasibility of controlling the molecular orientation and LRET of metalloproteins, by combining surface self-assembly chemistry, single-crystal electrochemistry, and scanning tunneling microscopy (STM).^{26–30} This has been followed by other later reports.^{31–37} In the present work, we combine environmentally friendly wet-chemical synthesis, two-dimensional (2D) surface assembly on well-defined, atomically

planar electrode surfaces, electrochemistry, and atomic force microscopy (AFM) to probe both the LRET and catalytic properties of PBNPs. We aim at controlling both ET and electrocatalysis, evaluating electrocatalytic efficiency at the single-nanoparticle level, and understanding the correlation between interfacial ET and electrocatalysis. Such a comprehensive approach to high-resolution PBNP surface dynamics in a well-defined microenvironment has not been reported before.

2. EXPERIMENTAL SECTION

The experimental details are provided in the [Supporting Information](#). The present section briefly summarizes the synthesis, characterization, and 2D surface assembly of PBNPs as well as the main instrumental methods.

2.1. Synthesis and Characterization of PBNPs. Pure PBNPs were obtained by a three-step procedure including synthesis of PB pigments, redispersion, and purification. The resulting nanoparticles were systematically characterized by spectroscopy and microscopy to map their morphology, size distribution, and stability.

2.2. Two-Dimensional Surface Assembly of PBNPs on Au(111) Surfaces. Single-crystal Au(111) electrodes were used as supporting substrates for both electrochemistry and AFM. To prepare SAMs on Au(111) electrode surfaces, the electrodes were annealed in a H₂ flame and quenched in ultrapure water saturated with H₂ gas. They were then immersed overnight in freshly prepared NH₂(CH₂)_nSH solutions (1–10 mM in ethanol). After rinsing with ethanol and Milli-Q water, the electrodes were transferred to PBNP aqueous solutions (around 2 mg mL⁻¹) and incubated at room temperature for several hours. Prior to use, the electrodes were rinsed with Milli-Q water.

2.3. Instrumental Methods. All electrochemical measurements were carried out at room temperature (23 ± 2 °C) using an Autolab System (Eco Chemie, The Netherlands) controlled by general-purpose electrochemical system software (GPES) or Nova 10. A three-electrode system was used, consisting of a reversible hydrogen electrode (RHE) as the reference electrode (RE), a platinum coiled wire as the counter electrode (CE), and a PBNP-NH₃⁺(CH₂)_nS-Au(111) electrode as the working electrode (WE). The RHE was freshly prepared just before measurements and checked against a saturated calomel electrode (SCE) after the measurements. All electrode potentials are referenced to the SCE. Purified argon (5 N, Chrompack, Varian) was applied to purge dioxygen from electrolyte solutions before the measurements, and an argon gas stream was maintained over the solution during the measurements.

AFM was performed using a 5500 AFM System (Agilent Technologies, Chandler, AZ) by AAC (acoustic alternating current) mode AFM, with the cantilever spring constant of oxide-sharpened Si₃N₄ probes (Bruker, SNL) 0.06 N m⁻¹. The tapping mode was mostly used, with a scan speed of 1.6 Hz and an amplitude of between 2.0 and 2.5 V. All AFM images in the figures are topographic images (512 pixels) and were recorded in the constant force mode using applied forces of 0.1–0.2 nN. The radius of the SNL tip is about 2 nm (according to the manufacturer's homepage). The scanner was calibrated by a Veeco 10 mm pitch calibration grating (each square with a 200 nm depth). All images for PBNP-NH₃⁺(CH₂)_nS-Au(111) systems were recorded in liquid environments (0.1 M KCl): i.e., the same environments as for electrochemical measurements.

3. RESULTS AND DISCUSSION

3.1. Synthesis, Characterization, and Electroactivity of PBNPs. Highly pure PBNP samples were prepared by a three-step procedure, detailed in the Supporting Information. This procedure represents an effective approach to obtain highly pure and stable PBNPs with relatively small sizes (<10 nm). The as-synthesized PBNPs are well dispersed in pure water or buffer solutions and have unusually high stability. The PBNPs prepared with the present method are in fact among the most stable to date for all NPs ever synthesized in liquid environments. After storage of the PBNP samples in pure water at room temperature even for 3.5 years, no aggregation or changes in physicochemical properties could be detected by

UV-vis spectroscopy, transmission electron microscopy (TEM), atomic force microscopy (AFM), or electrochemistry. The stability of PBNP suspensions were further checked in various chemical environments. In phosphate buffers (PBS; 10 mM), PBNPs are stable in the pH range of 5–8, which is compatible for their use in biosensing applications. In the presence of H₂O₂, the stability depends on the concentration of H₂O₂. At low concentrations (≤2 mM), the stability is not affected significantly: i.e., it is similar to that in pure water. When the H₂O₂ concentration is higher than 10 mM, the stability notably decreases to days. For long-term storage, we thus always suspend PBNPs in pure Milli-Q water.

The morphology, size distribution, and electroactivity were systematically characterized. UV-vis spectra show a strong maximum absorbance around 700 nm (Figure 1a and Figure S1 in the Supporting Information). Figure S1a,b shows the UV-vis spectra for different PBNP concentrations. The notion of fundamental absorbing units, Fe₄[Fe(CN)₆]₃, is addressed in the Supporting Information. The intensity is proportional to the PB concentration (Figure S1c,d), indicating that the PB spectral characteristics are retained for colloid PBNP dispersions, and the solubilized PBNPs behave as independent, noninteracting molecular-scale entities. The molar extinction coefficient, referenced to the formal molar concentration of stoichiometric Fe₄[Fe(CN)₆]₃ units, is 1.150 × 10³ L mol⁻¹ cm⁻¹. The blue color is associated with photoinduced charge transfer of Fe(II) → Fe(III) ET between largely localized single-center states,³⁸ classifying PB as a class II complex.^{39–42}

TEM and AFM images show that the PBNPs are spherical with an average size of ~6 nm (Figure 1b–d and Figure S2 in the Supporting Information). A single PBNP with the size emphasized is schematically illustrated in Figure 1e. This PBNP size is very close to that of horseradish peroxidase (HRP, Figure 1f), an enzyme crucial in electrochemical biosensors.^{43–46} The size distribution is fairly narrow (Figure 1c), with the fitting histogram of Figure 1d by Gaussian distribution size of 5.7 ± 0.3 nm of one PBNP, even though the preparation of monodisperse PBNPs remains a challenge.

PBNPs are highly electroactive, as proven by their electrochemical properties. We first recorded the voltammetry of PBNPs freely dispersed in solution. Well-defined cyclic voltammograms (CVs) were observed at both graphite (Figure S3 in the Supporting Information) and single-crystal Au(111) electrodes (Figure S4 in the Supporting Information). Graphite electrodes with a wide available potential window allow observing the full range of PBNP electroactivity, reflected by two pairs of redox peaks with formal potentials at 0.16 and 0.85 V (vs SCE) (Figure S3a,b), respectively. The pair at 0.16 V shows the higher electroactivity, while the pair of high-potential peaks has much weaker signals. The high-potential pair of redox peaks (at 0.85 V) can catalyze electrooxidation of H₂O₂, but with low efficiency.¹⁹ Most importantly, electrocatalytic H₂O₂ reduction is driven by the lower-potential pair of peaks around 0.16 V. It is well-known that one of the most important applications for PB is as an electron-transfer mediator for the fabrication of enzyme-based biosensors, which allows the detection of targeted analytes at low potentials to avoid redox interferences coming from compounds such as ascorbic and uric acids. In addition, this potential window is also the range appropriate for electrochemical studies using gold as the working electrode. In this work, our focus is thus on the 0.16 V peaks in catalytic electroreduction of H₂O₂. The linear dependence of both anodic and cathodic peak currents on

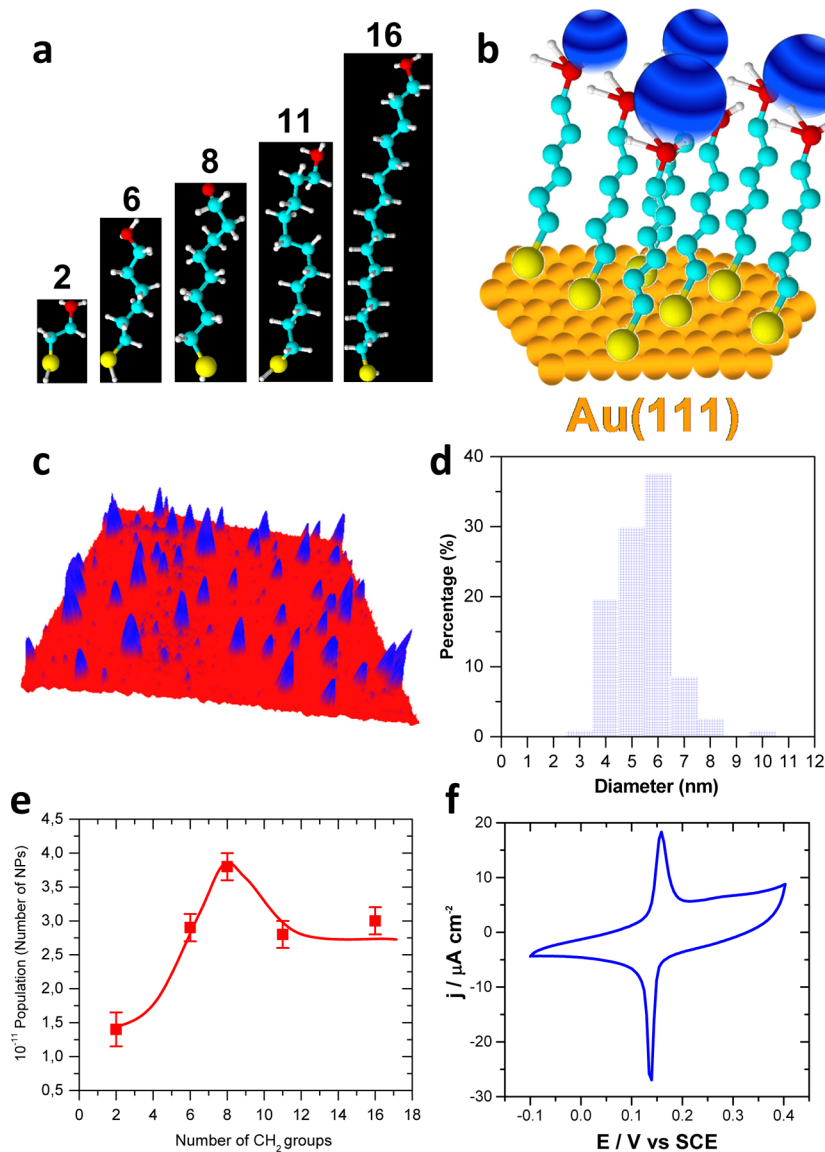


Figure 2. Two-dimensional surface assembly, characterization, and electroactivity of Prussian blue nanoparticles: (a) chemical structures of linking molecules drawn by Chemical Sketch with 3D structure optimization; (b) schematic representation of PBNPs self-assembled on SAM modified Au(111) surfaces; (c) 3D AFM image of PBNPs represented by the PBNP-NH₃⁺(CH₂)₆S-Au(111) system, acquired in the liquid environment; (d) histogram of the size distribution for immobilized PBNPs obtained from the measurements of PBNP heights in the AFM images; (e) dependence of the PBNP population on the chain length of linking molecules; (f) cyclic voltammograms obtained at the low scan rate of 0.1 V s⁻¹ for the PBNP-NH₃⁺(CH₂)₆S-Au(111) system. Electrolyte used in AFM imaging (c) and voltammetric measurements (f): 0.1 M KCl.

the square root of the scan rate indicates that the electrochemical reactions are diffusion-controlled (Figures S3c,d, and S4b) with no detectable adsorption of the PBNPs either on graphite or on an Au(111) electrode, largely due to the high solubility of PBNPs in aqueous solution. In short, the synthesized PBNPs retain the intrinsic electroactivity of PB and behave like redox macromolecules such as redox proteins in homogeneous solution.

3.2. 2D Surface Assembly and Controlled LRET. We employed molecular wiring self-assembly to confine PBNPs on Au(111) electrode surfaces. The linker molecules are amine-terminated alkanethiols with variable alkyl chain lengths (Figure 2a), which can form well-defined self-assembled monolayers (SAMs) via thiol-gold bonding chemistry.⁴⁷ Electrostatic interactions between the positively charged ammonium groups of the linking SAM and the negatively charged surface of the

PBNPs drive the 2D self-assembly of PBNPs into monolayer or submonolayer arrays (Figure 2b). We denote this system as PBNP-NH₃⁺(CH₂)_nS-Au(111), where *n* is the number of methylene groups in the alkyl chain (*n* = 2, 6, 8, 11, 16). The advantages of single-crystal Au(111) electrodes are that they offer low background current and highly ordered surface structure, facilitating the characterization and functional evaluation of the assembled PBNPs even at the single-NP level.

The 2D self-assembled PBNPs on Au(111) electrode surfaces were visualized by AFM in electrochemical environments (0.1 M KCl solution). AFM images were recorded over randomly chosen sample surface areas. A large number of AFM images in the tapping mode were acquired for all PBNP-NH₃⁺(CH₂)_nS-Au(111) systems (*n* = 2, 6, 8, 11, 16). Data for PBNP-NH₃⁺(CH₂)₆S-Au(111) are used as representatives. Figure 2c shows a representative AFM image, where isolated

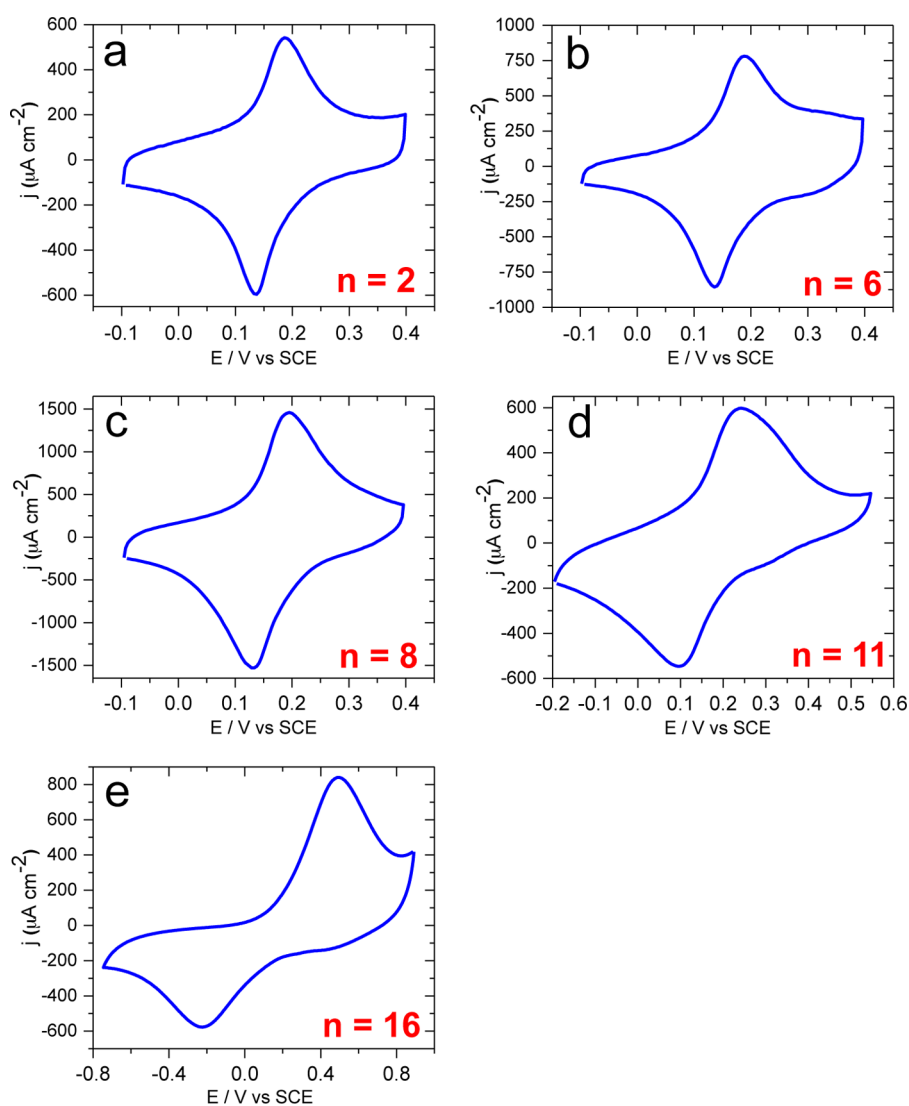


Figure 3. High-scan-rate cyclic voltammograms (CVs) of PBNP- $\text{H}_3\text{N}^+(\text{CH}_2)_n\text{S-Au(111)}$, obtained in 0.1 M KCl with the same scan rate of 5.0 V s^{-1} : (a) PBNP- $\text{H}_3\text{N}^+(\text{CH}_2)_2\text{S-Au(111)}$; (b) PBNP- $\text{H}_3\text{N}^+(\text{CH}_2)_6\text{S-Au(111)}$; (c) PBNP- $\text{H}_3\text{N}^+(\text{CH}_2)_8\text{S-Au(111)}$; (d) PBNP- $\text{H}_3\text{N}^+(\text{CH}_2)_{11}\text{S-Au(111)}$; (e) PBNP- $\text{H}_3\text{N}^+(\text{CH}_2)_{16}\text{S-Au(111)}$.

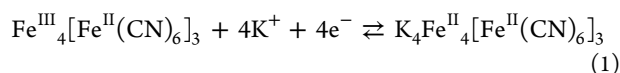
PBNPs are clearly imaged. The PBNP sizes were measured from the cross-section profiles. From the height histogram (Figure 2d), the mean diameter of the NPs is around 5–6 nm, consistent with the TEM data (Figure 1c,d). The size distribution of surface-confined PBNPs is in fact narrower than that measured by TEM (comparison of Figure 2d with Figure 1d), most likely due to selective surface-induced adsorption where similar sized nanoparticles are favored to form a 2D pattern. AFM images of other systems are given in the Supporting Information (e.g., Figure S5). The results clearly show that self-assembled PBNPs were well attached to the Au (111) surfaces and stable in the electrochemical environments.

The PBNP population was estimated by statistical AFM analysis. The average number of PBNPs per unit area was taken as the surface coverage.⁴⁸ Quantifying the number of surface-bound particles by AFM is a challenge (or even misleading) without careful corrections for AFM convolution.⁴⁹ We used a simple but rational model,⁵⁰ where all the particles were assumed to be of regular spherical shape. The maximum surface coverage could then be obtained by assuming that the surface is

fully covered with a close-packed NP monolayer. The accurate surface coverage is calculated as the percentage of apparent NP population vs maximum population in a given surface area (e.g., $2 \mu\text{m} \times 2 \mu\text{m}$). The analysis showed that the PBNP population on $\text{NH}_3^+(\text{CH}_2)_n\text{S-Au(111)}$ surfaces increases with increasing linker molecular length and reaches a maximum at $n = 8$ (Figure 2e). This observation was compared with the electrochemical results and is further discussed below.

Following AFM imaging and statistical analysis, we recorded electrochemical data for the immobilized PBNPs. A CV of the PBNPs- $\text{NH}_3^+(\text{CH}_2)_6\text{S-Au(111)}$ system as a representative is shown in Figure 2f, with a pair of sharp redox peaks around 0.15 V. CVs at different scan rates are provided in Figure S6a in the Supporting Information. Both anodic and cathodic peak currents increase linearly with increasing scan rate (Figure S6b), indicating that the PBNPs exhibit diffusionless electrochemical reactions.⁵¹

The sharp peaks, with very narrow anodic and cathodic half-peak widths, are strongly indicative of an interfacial multi-ET process (Figure 2f). The electrochemical reaction can be represented as



An apparent four-ET process (eq 1) has long been recognized for PB-related electrochemistry,^{16–21} but a four-ET process raises concerns regarding the microscopic nature of such a process. The environmental reorganization free energy thus rises strongly with the number of electrons transferred in a single step (as the square of this number). Multi-ET is therefore disfavored, unless unstable radical states are formed in single-ET steps. The 5–6 nm PBNPs seem to behave differently. Details of the PBNP multi-ET process are presently unresolved, but two suggestions can be forwarded. One is that counterions bound to the negatively charged PBNPs significantly increase the effective particle radius. This would at least diminish prohibitive multi-ET environmental reorganization barriers. Solvent structural effects (e.g., nonlocal dielectric solvent effects) further attenuate the solvent dynamics. The other, more palatable suggestion is that the large number of mixed-valence Fe(II)/Fe(III) redox units imposes collective properties on the PBNPs. With the PBNP size, successive single-ET charging energy gaps are small ($\ll k_{\text{B}}T$ where k_{B} is Boltzmann's constant and T the temperature) and the redox potentials of successive single-ET steps therefore very close. Other data generally related to electronic and conductivity properties of PB and PB analogues can be found in a comprehensive report and references therein.⁴²

Other chain lengths are in accord with behavior similar to that of C_6 , which supports the generality of this voltammetric pattern. In all cases, anodic and cathodic Faradaic signals correspond to eq 1.^{16–23} The formal PBNP redox potential ($E^{\circ'}$) is almost independent of the alkyl chain length for short chains (Table S1 in the Supporting Information) and is around 0.15 V vs SCE but is shifted to slightly more positive values for longer chain lengths. However, this effect is small, most likely arising from the more rigid orientation of PBNPs on longer chain SAMs.

It is noted from Table S1 in the Supporting Information that the surface coverage of PBNPs estimated from voltammetry first increases with increasing chain length and then passes a maximum. This observation follows the AFM population analysis and suggests that the stability of the PBNP adlayer is enhanced by increasing alkyl chain length. The packing order of the monolayer on the electrode surface thus first increases with increasing alkyl chain length, in accordance with other observations for long-chain alkanethiol SAMs.^{52,53} As for the AFM population statistics (Figure 2e), this effect reaches saturation at a chain length of about eight methylene groups, but the outcomes from the two methods reflect different physical properties. The AFM images count the number of PBNPs. Voltammetry measures the number of active PBNP redox units (eq 1). By comparing the two results, we are able to calculate the number of effective redox units per PBNP (Table S2 in the Supporting Information). This number is consistently around 21–28 units, with a slightly increasing value as the molecular chain length increases. To the best of our knowledge, this is the first time that the numbers of active units for structurally complex NPs such as PBNPs have been determined, which sets a solid basis for probing electrocatalytic efficiency at the single-NP level (see section 3.3).

The systems are highly stable toward fast voltammetry (up to 300 V s⁻¹), enabling us to disentangle the ET kinetics.

Variation of the CVs with increasing alkyl chain length is reflected by the peak separation and shape (e.g., Figure 3 and Figure S7 in the Supporting Information), both indicative of strongly distance dependent ET kinetics. To obtain interfacial ET rate constants (k_{s}), a series of CVs with different scan rates (e.g., 1–300 V s⁻¹) for each system were recorded. The data were analyzed on the basis of Laviron's method,⁵⁴ using eq 2^{54b}

$$m = \frac{RT k_{\text{s}}}{nF v} \quad (2)$$

where m is a parameter determined by the peak separation obtained from the CVs, n is the number of electrons transferred, v is the scan rate, F is the Faraday constant, and the other symbols have their usual meaning. Thus, the rate constant can be estimated from the slope of the plot of m vs $1/v$. As an example, the linear relation between the Laviron parameter m^{-1} and scan rate (v) for the PBNP-NH₃⁺(CH₂)₆S-Au(111) system is shown in Figure S8 in the Supporting Information. The rate constants for the different layers investigated are summarized in Table 1. The ET rate constant

Table 1. Comparison of Electron-Transfer Rates and Electrocatalytic Efficiency of PBNPs Attached to Au(111) Surfaces via Various Chain Length Alkanethiols

| PBNP- H ₃ N ⁺ (CH ₂) _n S- Au(111) | ET rate constant k_{s} (s ⁻¹) | catalytic current per nanoparticle (10 ¹² _{cat} (μA)) |
|--|---|--|
| $n = 2$ | 1706 | 46.9 |
| $n = 6$ | 1166 | 29.4 |
| $n = 8$ | 599 | 24.7 |
| $n = 11$ | 15 | 18.7 |
| $n = 16$ | 0.4 | 5.1 |

(k_{s}) dependence on the PBNPs/electrode surface distance (Figure 4a) is in accord with eq 3 for the longer chains

$$k_{\text{s}} = k_0 \exp(-\beta n) \quad (3)$$

where k_0 is the rate constant when $n = 0$, β is the decay factor, and n is the distance between the PBNPs and the electrode surface (number of C atoms in the linker molecules). The rate constant is largely independent of the chain length up to six methylene groups ($n = 6$). A clear exponential decay with a decay factor of $\beta = 0.85$ per CH₂ (equivalent to ca. 0.7 Å⁻¹), strongly indicative of electron tunneling through the alkanethiol SAM, is observed only for longer chain lengths. This bimodal distance dependence is also encountered for electrochemical ET of the redox metalloproteins azurin²⁷ and cytochromes c^{55} and c_4 ,⁵⁶ which is explained by a dynamic configurational prearrangement (“gated” ET) of protein molecules²⁷ or, in the present case, PBNPs.

3.3. Electrocatalytic Activity and Correlation with Interfacial ET Kinetics. One of the most important functions of PB materials is their *selective* and *strong* electrocatalysis in the reduction of hydrogen peroxide,^{16–22} the electrocatalytic cycle of which is illustrated in Figure S9 in the Supporting Information. The electrocatalysis of H₂O₂ reduction by immobilized PBNPs on all linkers was evaluated systematically by CV. As a representative, a comparison of CVs at PBNPs-NH₃⁺(CH₂)₆S-Au(111) electrodes and at a reference NH₃⁺(CH₂)₆S-Au(111) system clearly shows that the PBNPs are strong electrocatalysts (Figure 4b). H₂O₂ electroreduction starts at the significantly positive potential of 0.3 V (vs SCE)

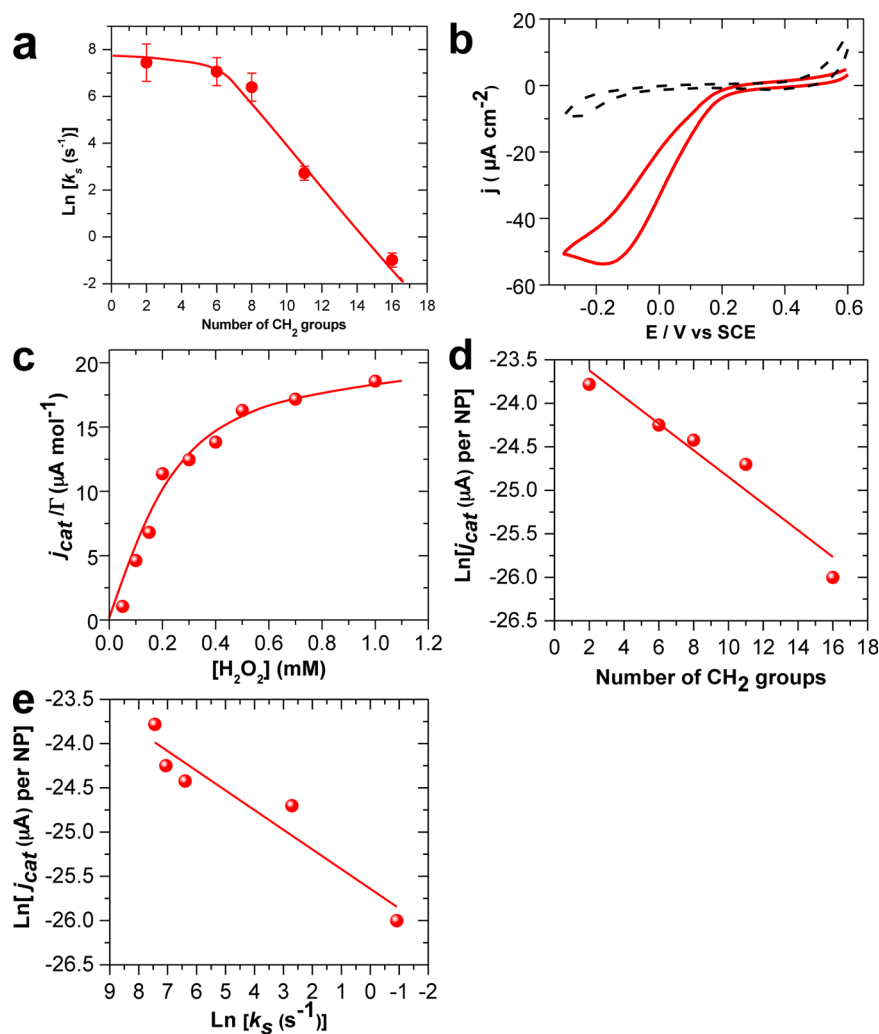


Figure 4. Electron transfer pattern and enzyme-like electrocatalysis of immobilized PBNPs: (a) correlation of the apparent electron transfer rate constants with the distance denoted by the number of methylene units in the linking molecules in the absence of H_2O_2 substrate; (b) comparison of cyclic voltammograms obtained at PBNP- $\text{NH}_3^+(\text{CH}_2)_6\text{S-Au}(111)$ (red curve) and $\text{NH}_3^+(\text{CH}_2)_6\text{S-Au}(111)$ (black curve, i.e. without PBNPs) surface systems (experimental conditions: 0.1 M KCl as electrolyte, concentration of H_2O_2 0.5 mM and scan rate 20 mV s^{-1}); (c) correlation of the electrocatalytic current with H_2O_2 concentration; (d) dependence of electrocatalytic current generated by a single PBNP on the ET distance; (e) possible correlation of electrocatalytic current per PBNP with the electron transfer rate constant.

and reaches a current maximum at about -0.1 V (red curve, Figure 4b). Only very small currents were detected at potentials more negative than -0.1 V for the control system (black dashed curve, Figure 4b).

Our further analysis is based on observed currents at a fixed potential of -0.05 V , for $[\text{H}_2\text{O}_2]$ in the $0.05\text{--}1 \text{ mM}$ range. The immobilized PBNP SAMs are stable for successive amperometric measurements to record the time–current ($i\text{--}t$) curves, even at high H_2O_2 concentrations up to 5 mM . An example for PBNP- $\text{NH}_3^+(\text{CH}_2)_6\text{S-Au}(111)$ is shown in Figure 4c. The current first increases with increasing $[\text{H}_2\text{O}_2]$ with a linear correlation up to 0.3 mM and then tends toward a constant value above 0.8 mM H_2O_2 , attributed to substrate saturation. This resembles the behavior of an enzymatic (electro)catalytic reaction. We therefore use the electrochemical versions of the Michaelis–Menten and Lineweaver–Burk formalism to analyze the data. The electrochemical Michaelis–Menten equation is a correlation between the electrocatalytic current density (j_{cat}) and the substrate concentration ($[\text{S}]$). Use of this equation needs modification when we explicitly include the tunneling ET

step between the PBNPs and the electrode surface. We use first the form

$$j_{\text{cat}} = nF\Gamma v_{\text{cat}}([\text{S}]) \text{ or } v_{\text{cat}}([\text{S}]) = \frac{k_{\text{cat}}[\text{S}]}{K_{\text{M}} + [\text{S}]} \quad (4)$$

where Γ is the surface PBNP coverage, n the number of electrons transferred (here $n = 4$), F the Faraday constant, K_{M} the apparent Michaelis constant, and k_{cat} the apparent catalytic turnover rate. Since the effective PBNP surface coverage could be estimated from the voltammetric data (Table S1 in the Supporting Information), we were able to fit the experimental data using eq 3 (the dots in Figure 4c). The best fit was obtained for $K_{\text{M}} = 0.29 \pm 0.03 \text{ mM}$ and $k_{\text{cat}} = 63 \pm 4 \text{ s}^{-1}$ (the solid lines in Figure 4c).

The same data were also analyzed by the Lineweaver–Burk equation (eq 5)

$$\frac{1}{j_{\text{cat}}/\Gamma} = \frac{1}{nFk_{\text{cat}}} + \frac{K_{\text{M}}}{nFk_{\text{cat}}} \frac{1}{[\text{S}]} \quad (5)$$

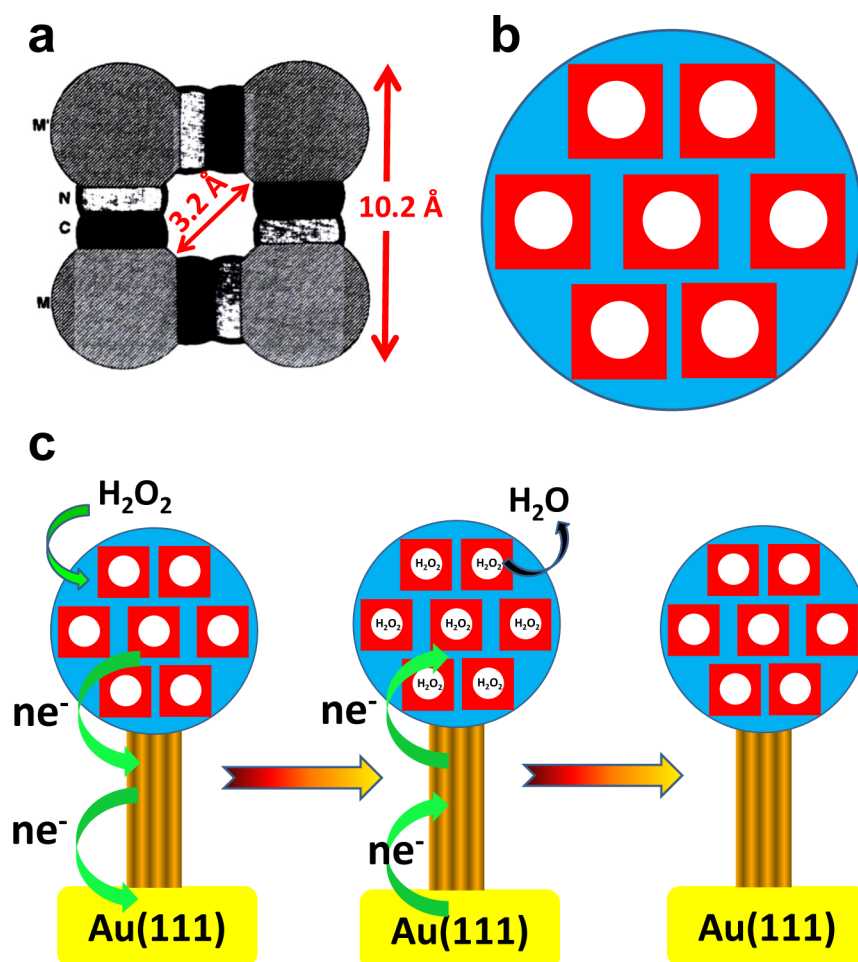


Figure 5. Proposed structures and electrocatalytic mechanisms of PBNPs: (a) unit cell structure of PB crystals with a cubic cell of 10.2 Å containing a 3.2 Å binding channel; (b) schematic illustration of a single PBNP consisting of multiple structural units (or redox units); (c) schematic representations of substrate binding, electron transfer, and electrocatalysis of PBNPs immobilized on Au(111) surfaces. Parts (b) and (c) are not drawn to scale.

from which K_M and k_{cat} were found to be 0.16 ± 0.05 mM and 52 ± 4 s⁻¹, respectively. Therefore, the values from Michaelis–Menten and Lineweaver–Burk plots both make sense, as different fitting procedures (nonlinear and linear) are used. The nonlinear Michaelis–Menten fitting would be more accurate for our system, as even small errors in electrocatalytic current density would lead to large errors in the parameters of the reciprocal Lineweaver–Burk form.

The smaller the K_M value, the higher the substrate binding affinity. PBNPs show a K_M value as small as 0.16 mM (or 0.29 mM), comparable with the substrate binding affinity of many natural peroxidases. For example, the Michaelis constant toward H₂O₂ binding of free horseradish peroxidase (HRP, Figure 1f) is in the range 0.2–3.7 mM in homogeneous solution.^{57,58} When HRP is immobilized on solid surfaces, K_M varies significantly from 0.3 to 5 mM, depending on the support materials.⁵⁸ PBNPs thus have H₂O₂ binding affinity comparable to or even higher than that of HRP, most likely due to multiple binding sites in PBNP in contrast to a single binding site in HRP. In short, we have introduced an electrocatalytic system: i.e. the PBNPs are immobilized on highly well-defined electrode surfaces in a sophisticated way. The biomimetic features are reflected by these physicochemical characteristics. (a) The catalytic centers, i.e. the PBNPs, have approximately the same structural size as real enzymes and catalyze the same process,

i.e. H₂O₂ reduction, as real enzymes (the peroxidases) with comparable efficiency. (b) As expected, PB material has well been proven to have high selectivity toward the electrocatalytic reduction of H₂O₂. (c) The high affinity of PBNPs for H₂O₂ is well indicated by a small K_M value at around 0.2 mM which is comparable to or even smaller than that for a natural peroxidase such as HRR.

The electrocatalytic efficiency was evaluated by the average current per PBNP obtained from the combined AFM and voltammetry data (Table 1) and then correlated with the variable-distance interfacial ET kinetics at the SAM-modified Au(111) electrode surfaces. Two types of plots are compared in Figure 4d,e and Figures S11 and S12 in the Supporting Information. The catalytic current per PBNP particle, $j_{\text{cat}}^{\text{tot}}$, was plotted either against the linker molecular chain length or against the logarithm of the interfacial ET rate constant, $\ln k_s$. A bimodal linear dependence is observed for both cases (Figure S11a and S12a), but the dependence of $j_{\text{cat}}^{\text{tot}}$ on the molecular linker chain length is much weaker (Figure S11b) than for the ET rate constant (k_s) (Figure 4a). $j_{\text{cat}}^{\text{tot}}$ thus decreases approximately linearly with increasing ET distance (Figure S11b), while k_s decays exponentially (Figure 4a).

This difference is understandable from the following analysis.^{59,60} The overall electrocatalytic process is considered as a two-step process rather than as the single-step process in

eqs 4 and 5. The two steps involve catalytic reduction of H_2O_2 on the PBNP and LRET between the PBNP and the electrode surface via the SAM. The two-step mechanism can be represented by eq 6.

$$j_{\text{cat}}^{\text{tot}} = nF\Gamma \frac{k_s v_{\text{cat}}([S])}{k_{-s} + v_{\text{cat}}([S])} \quad (6)$$

Most of these symbols were defined above, but k_s now takes the form

$$k_s = k_0 \exp\left(-\frac{\alpha e\eta}{k_B T}\right) \exp(-\beta n) \quad (7)$$

i.e. k_s in eq 7 is now the rate constant at the overpotential η where electrocatalysis was recorded and differs from k_s determined by the Laviron analysis which refers to the equilibrium potential ($\eta = 0$). α is the electron transfer coefficient and k_{-s} the electrochemical ET rate constant for the reverse process.

$$k_{-s} = k_0 \exp\left(-\frac{(1-\alpha)e\eta}{k_B T}\right) \exp(-\beta n) \quad (8)$$

A combination of eqs 3 and 6–8 gives the following transparent $j_{\text{cat}}^{\text{tot}}$ forms

$$j_{\text{cat}}^{\text{tot}} = nF\Gamma \frac{1}{\exp(e\eta/k_B T) \frac{1}{v_{\text{cat}}([S])} - \ln k_{s0} + \beta n} \quad \text{or}$$

$$\frac{j_{\text{cat}}^{\text{tot}}}{nF\Gamma} = \frac{1}{v_{\text{cat}}([S])} \exp(e\eta/k_B T) - \ln k_{s0} + \beta n \quad (9)$$

$j_{\text{cat}}^{\text{tot}}$ or $1/j_{\text{cat}}^{\text{tot}}$ can be plotted against n as in eq 9. We cannot immediately plot $j_{\text{cat}}^{\text{tot}}$ or $1/j_{\text{cat}}^{\text{tot}}$ against k_s , since k_s under electrocatalytic conditions is not the same as that estimated above for ET conditions due to the different electrochemical potentials used.

We note that from eq 6

$$j_{\text{cat}}^{\text{tot}} \approx e\Gamma k_s$$

$$= e\Gamma k_{s0} \exp(-\alpha e\eta/k_B T) \exp(-\beta n)$$

when $k_s \ll k_{\text{cat}}$ (10)

and we recover the exponential dependence on n . This is expected for long chains (Figure 4d,e). In the opposite limit, when $k_s \gg k_{\text{cat}}$

$$j_{\text{cat}}^{\text{tot}} \approx nF\Gamma \frac{k_s}{k_{-s}} v_{\text{cat}}([S]) = nF\Gamma \exp(-\alpha e\eta/k_B T) v_{\text{cat}}([S]) \quad (11)$$

i.e. with no dependence of $j_{\text{cat}}^{\text{tot}}$ on n . As for the interfacial ET process, the distance dependence of the combined ET and electrocatalytic control is again bimodal. The weak distance dependence and the close accordance with the Michaelis–Menten and Lineweaver–Burk analysis suggest further that the limit represented by eq 11 prevails for the overpotential and distance (six carbon atoms) used for the Michaelis–Menten and Lineweaver–Burk analyses. This observation is in accord again with the data in Figure 4a. Exponential and linear distance decays are in fact indistinguishable for weakly distance dependent currents. The observed weak dependence therefore

suggests that the PBNP electrocatalysis corresponds to a distance range between the two limits in eqs 10 and 11.

3.4. Proposed Nanoparticle Structures and Electrocatalytic Mechanisms. As noted, H_2O_2 binds strongly to PBNPs. This must originate in the PBNP intrinsic structure. Although the 3D crystallographic structure of individual PBNPs is not available, we can suggest the schematic views in Figure 5. PB is known from X-ray analysis to form a polynuclear network of well-defined unit cells (Figure S13 in the Supporting Information).^{61,62} The 10.2 Å cubic unit cell contains a 3.2 Å channel⁵⁷ (Figure 5a) believed to act as a pseudoselective binding site for small molecules such as O_2 and H_2O_2 . While the unit cell volume is only 1.06 nm³, the volume of a 6 nm PBNP can be as large as 112.6 nm³. A single PBNP can thus contain up to 106 unit cells, and a PBNP could in principle contain as many as 106 binding sites for H_2O_2 (Figure 5b). This number was presently found to be 21–28 effective redox units per PBNP (Table S2 in the Supporting Information) from electrochemical and AFM data, suggesting that approximately 21% of the structural units in a PBNP are involved in electrocatalysis (Figure 5c). Only surface redox units thus seem active for electrocatalysis, but it should be noted that the redox units are not necessarily the same as the crystal structure units.

4. CONCLUSIONS

We have used Prussian blue nanoparticles (PBNPs) as a representative of electroactive NPs to study controlled nanoscale ET and electrocatalysis and to explore correlations between electrocatalytic efficiency and interfacial ET kinetics. Several interesting outcomes are (1) a facile wet-chemical approach that enables synthesizing extremely stable PBNP dispersions, (2) mixed-valence NPs that show high electroactivity and behave similarly to redox metalloproteins such as the blue copper protein azurin and the heme proteins cytochrome *c* and *c*₄, (3) PBNPs with high binding affinity toward H_2O_2 and enzyme-like electrocatalysis in a two-step reaction mode that involves interfacial ET between the PBNP and the electrode surface and PBNP catalyzed H_2O_2 reduction, and (4) a weak dependence of electrocatalytic efficiency on interfacial ET distance, indicative that the two-step electrocatalytic currents are simultaneously controlled by interfacial ET and PBNP-catalyzed H_2O_2 conversion.

The 3D crystallographic structures of the NPs would be essential for fully understanding interfacial ET and electrocatalysis. This remains a daunting challenge for most types of NPs, and only very few reports are available. The most convincing case is thiol-monolayer-protected gold clusters, for which X-ray crystal resolution has reached 1.15 Å.⁶³ Such analysis is more challenging for multicomponent NPs such as PBNPs, because of their complex structure and the technical difficulty in preparing monodisperse NPs and NP single crystals suitable for X-ray crystallography. Ongoing efforts could thus focus on preparing uniformly sized PBNPs and growing large-size PBNP-based single crystals.

■ ASSOCIATED CONTENT

Supporting Information

The Supporting Information is available free of charge on the ACS Publications website at DOI: 10.1021/acscatal.6b00411.

Experimental details, photographs of the samples, UV–vis spectra, additional electrochemical data, and AFM images (PDF)

AUTHOR INFORMATION

Corresponding Author

*E-mail for Q.C.: cq@kemi.dtu.dk.

Notes

The authors declare no competing financial interest.

ACKNOWLEDGMENTS

We acknowledge financial support by the Danish Research Council for Technology and Product Sciences (Project No. 12-12744, to Q.C.) and the Lundbeck Foundation (Grant No. R49-A5331, to Q.C.). N.Z. acknowledges the NanoScience Center at the University of Copenhagen and Nano-DTU for a Ph.D. fellowship. X.H. acknowledges Universities Denmark for a postdoctoral fellowship.

REFERENCES

- (1) Pelaz, B.; Jaber, S.; de Aberasturi, D. J.; Wulf, V.; Aida, T.; de la Fuente, J. M.; Feldmann, J.; Gaub, H. E.; Josephson, L.; Kagan, C. R.; Kotov, N. A.; Liz-Marzan, L. M.; Mattoussi, H.; Mulvaney, P.; Murray, C. B.; Rogach, A. L.; Weiss, P. S.; Willner, I.; Parak, W. J. *ACS Nano* **2012**, *6*, 8468–8483.
- (2) Wei, H.; Wang, E. K. *Chem. Soc. Rev.* **2013**, *42*, 6060–6093.
- (3) Tang, Z. Y.; Wang, Y.; Podsiadlo, P.; Kotov, N. A. *Adv. Mater.* **2006**, *18*, 3203–3224.
- (4) Park, J.; Nguyen, T. D.; Silveira, G. D.; Bahng, J. H.; Srivastava, S.; Zhao, G. P.; Sun, K.; Zhang, P. J.; Glotzer, S. C.; Kotov, N. A. *Nat. Commun.* **2014**, *5*, 3593.
- (5) Zayats, M.; Baron, R.; Popov, I.; Willner, I. *Nano Lett.* **2005**, *5*, 21–25.
- (6) Xiao, Y.; Pavlov, V.; Levine, S.; Niazov, T.; Markovitch, G.; Willner, I. *Angew. Chem., Int. Ed.* **2004**, *43*, 4519–4522.
- (7) Francke, R.; Little, R. D. *Chem. Soc. Rev.* **2014**, *43*, 2492–2521.
- (8) Lund, H. J. *Solid State Electrochem.* **2011**, *15*, 1733–1751.
- (9) Zaltis, C. M.; Kramer, D.; Kucernak, A. R. *Phys. Chem. Chem. Phys.* **2013**, *15*, 4329–4340.
- (10) Shih, Z. Y.; Wang, C. W.; Xu, G. B.; Chang, H. T. *J. Mater. Chem. A* **2013**, *1*, 4773–4778.
- (11) Hill, M. G.; Barton, J. K.; Boon, E. M.; Ceres, D. M.; Drummond, T. G. *Nat. Biotechnol.* **2000**, *18*, 1096–1100.
- (12) Lapiere, M. A.; O’Keefe, M.; Taft, B. J.; Kelley, S. O. *Anal. Chem.* **2003**, *75*, 6327–6333.
- (13) Siahrostami, S.; Verdaguer-Casadevall, A.; Karamad, M.; Deiana, D.; Malacrida, P.; Wickman, B.; Escudero-Escribano, M.; Paoli, E. A.; Frydendal, R.; Hansen, T. W.; Chorkendorff, I.; Stephens, I. E. L.; Rossmeisl, J. *Nat. Mater.* **2013**, *12*, 1137–1143.
- (14) Hernandez-Fernandez, P.; Masini, F.; McCarthy, D. N.; Strelbel, C. E.; Friebe, D.; Deiana, D.; Malacrida, P.; Nierhoff, A.; Bodin, A.; Wise, A. M.; Nielsen, J. H.; Hansen, T. W.; Nilsson, A.; Stephens, I. E. L.; Chorkendorff, I. *Nat. Chem.* **2014**, *6*, 732–738.
- (15) Studt, F.; Sharafutdinov, I.; Abild-Pedersen, F.; Elkjaer, C. F.; Hummelshøj, J. S.; Dahl, S.; Chorkendorff, I.; Nørskov, J. K. *Nat. Chem.* **2014**, *6*, 320–324.
- (16) Neff, V. D. *J. Electrochem. Soc.* **1978**, *125*, 886–887.
- (17) Itaya, K.; Shoji, N.; Uchida, I. *J. Am. Chem. Soc.* **1984**, *106*, 3423–3429.
- (18) Itaya, K.; Uchida, I.; Neff, V. D. *Acc. Chem. Res.* **1986**, *19*, 162–168.
- (19) Chi, Q. J.; Dong, S. J. *Anal. Chim. Acta* **1995**, *310*, 429–436.
- (20) Karyakin, A. A. *Electroanalysis* **2001**, *13*, 813–819.
- (21) Ricci, F.; Paleschi, G. *Biosens. Bioelectron.* **2005**, *21*, 389–407.
- (22) Zolotukhina, E. V.; Bezverkhy, I. S.; Vorotyntsev, M. A. *Electrochim. Acta* **2014**, *122*, 247–258.
- (23) Liu, S. Q.; Xu, J. J.; Chen, H. Y. *Electrochem. Commun.* **2002**, *4*, 421–425.
- (24) Fiorito, P. A.; Goncales, V. R.; Ponzio, E. A.; de Torresi, S. I. C. *Chem. Commun.* **2005**, *3*, 366–368.
- (25) Zolotukhina, E. V.; Vorotyntsev, M. A.; Bezverkhy, I. S.; Borisova, A. V.; Karyakin, A. A.; Zolotov, Y. A. *Dokl. Phys. Chem.* **2012**, *444*, 75–78.
- (26) Chi, Q. J.; Zhang, J. D.; Nielsen, J. U.; Friis, E. P.; Chorkendorff, I.; Canters, G. W.; Andersen, J. E. T.; Ulstrup, J. *J. Am. Chem. Soc.* **2000**, *122*, 4047–4055.
- (27) Chi, Q. J.; Zhang, J. D.; Andersen, J. E. T.; Ulstrup, J. *J. Phys. Chem. B* **2001**, *105*, 4669–4679.
- (28) Chi, Q. J.; Farver, O.; Ulstrup, J. *Proc. Natl. Acad. Sci. U. S. A.* **2005**, *102*, 16203–16208.
- (29) Della Pia, E. A.; Chi, Q. J.; Jones, D. D.; Macdonald, J. E.; Ulstrup, J.; Elliott, M. *Nano Lett.* **2011**, *11*, 176–182.
- (30) Della Pia, E. A.; Chi, Q. J.; Macdonald, J. E.; Ulstrup, J.; Jones, D. D.; Elliott, M. *Nanoscale* **2012**, *4*, 7106–7113.
- (31) Fujita, K.; Nakamura, N.; Ohno, H.; Leigh, B. S.; Niki, K.; Gray, H. B.; Richards, J. H. *J. Am. Chem. Soc.* **2004**, *126*, 13954–13961.
- (32) Bonanni, B.; Andolfi, L.; Bizzarri, A. R.; Cannistraro, S. *J. Phys. Chem. B* **2007**, *111*, 5062–5075.
- (33) Zhang, Z. L.; Pang, D. W.; Zhang, R. Y.; Yan, J. W.; Mao, B. W.; Qi, Y. P. *Bioconjugate Chem.* **2002**, *13*, 104–109.
- (34) Nakano, K.; Yoshitake, T.; Yamashita, Y.; Bowden, E. F. *Langmuir* **2007**, *23*, 6270–6275.
- (35) Eckermann, A. L.; Feld, D. J.; Shaw, J. A.; Meade, T. J. *Coord. Chem. Rev.* **2010**, *254*, 1769–1802.
- (36) Myers, C. P.; Williams, M. E. *Coord. Chem. Rev.* **2010**, *254*, 2416–2428.
- (37) Dai, P. X.; Chen, T.; Wang, D.; Wan, L. J. *J. Phys. Chem. C* **2012**, *116*, 6208–6214.
- (38) Robin, M. B. *Inorg. Chem.* **1962**, *1*, 337–342.
- (39) Allen, G. C.; Hush, N. S. *Prog. Inorg. Chem.* **1967**, *8*, 357–389.
- (40) Hush, N. S. *Prog. Inorg. Chem.* **1967**, *8*, 391–433.
- (41) Mayoh, B.; Day, P. J. *Chem. Soc., Dalton Trans.* **1976**, 1483–1486.
- (42) Behera, J. N.; D’Alessandro, D. M.; Soheilnia, N.; Long, J. R. *Chem. Mater.* **2009**, *21*, 1922–1926.
- (43) Ruzgas, T.; Csoregi, E.; Emneus, J.; Gorton, L.; MarkoVarga, G. *Anal. Chim. Acta* **1996**, *330*, 123–138.
- (44) Ferapontova, E. E. *Electroanalysis* **2004**, *16*, 1101–1112.
- (45) Kartashov, A. V.; Serafini, G.; Dong, M. D.; Shipovskov, S.; Gazaryan, I.; Besenbacher, F.; Ferapontova, E. E. *Phys. Chem. Chem. Phys.* **2010**, *12*, 10098–10107.
- (46) Chen, W.; Cai, S.; Ren, Q. Q.; Wen, W.; Zhao, Y. D. Recent advances in electrochemical sensing for hydrogen peroxide: a review. *Analyst* **2012**, *137*, 49–58.
- (47) Zhang, J. D.; Bilic, A.; Reimers, J. R.; Hush, N. S.; Ulstrup, J. *J. Phys. Chem. B* **2005**, *109*, 15355–15367.
- (48) Zhao, J.; Zhu, X. L.; Li, T.; Li, G. X. *Analyst* **2008**, *133*, 1242–1245.
- (49) Geronimo, C. L. A.; MacCuspie, R. I. *Microsc. Microanal.* **2011**, *17*, 206–214.
- (50) Hao, Y. Master’s Thesis, Technical University of Denmark, DK-2800 Kongens Lyngby, Denmark, 2009.
- (51) Bard, A. J.; Faulkner, L. N. *Electrochemical Methods*, 2nd ed.; Wiley: Chichester, U.K., 2001; pp 87–155.
- (52) Hong, H. G.; Park, W. *Langmuir* **2001**, *17*, 2485–2492.
- (53) Porter, M. D.; Bright, T. B.; Allara, D. L.; Chidsey, C. E. D. *J. Am. Chem. Soc.* **1987**, *109*, 3559–3568.
- (54) (a) Laviro, E. J. *Electroanal. Chem. Interfacial Electrochem.* **1979**, *101*, 19–28. (b) Jensen, P. S.; Chi, Q.; Grummen, F. B.; Abad, J. M.; Horsewell, A.; Schiffrin, D. J.; Ulstrup, J. *J. Phys. Chem. C* **2007**, *111*, 6124–6132.
- (55) Song, S.; Clark, R. A.; Bowden, E. F.; Tarlov, M. J. *J. Phys. Chem.* **1993**, *97*, 6564–6572.
- (56) Chi, Q.; Zhang, J. D.; Arslan, T.; Borg, L.; Pedersen, G. W.; Christensen, H. E. M.; Nazmudtinov, R. R.; Ulstrup, J. *J. Phys. Chem. B* **2010**, *114*, 5617–5624.
- (57) Patel, A. C.; Li, S. X.; Yuan, J. M.; Wei, Y. *Nano Lett.* **2006**, *6*, 1042–1046.

- (58) Ikemoto, H.; Chi, Q. J.; Ulstrup, J. *J. Phys. Chem. C* **2010**, *114*, 16174–16180.
- (59) Karyakin, A. A.; Karyakina, E. E.; Gorton, L. *J. Electroanal. Chem.* **1998**, *456*, 97–104.
- (60) Karyakin, A. A.; Karyakina, E. E.; Gorton, L. *Electrochem. Commun.* **1999**, *1*, 78–82.
- (61) Buser, H. J.; Schwarzenbach, D.; Petter, W.; Ludi, A. *Inorg. Chem.* **1977**, *16*, 2704–2710.
- (62) Herren, F.; Fischer, P.; Ludi, A.; Halg, W. *Inorg. Chem.* **1980**, *19*, 956–959.
- (63) Jadzinsky, P. D.; Calero, G.; Ackerson, C. J.; Bushnell, D. A.; Kornberg, R. D. *Science* **2007**, *318*, 430–433.